

Synthesis of High-Entropy Alloys with a Tailored Composition and Phase Structure Using a Single Configurable Target

Khurshed Alam,¹ Woohyung Jang,¹ Geonwoo Jeong, Jinhui Ser, Door Kang, Tae-Hoon Kim,* and Hoonsung Cho*



Cite This: *ACS Omega* 2024, 9, 1362–1374



Read Online

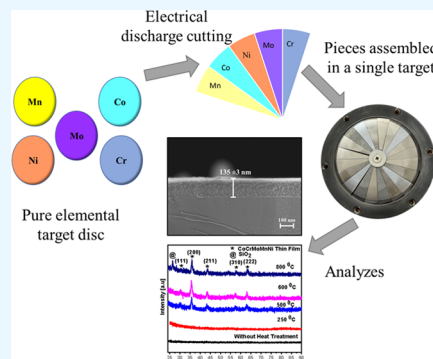
ACCESS |

Metrics & More

Article Recommendations

Supporting Information

ABSTRACT: Previously, refractory high-entropy alloys (HEAs) with high crystallinity were synthesized using a configurable target without heat treatment. This study builds upon prior investigations to develop nonrefractory elemental HEAs with low crystallinity using a novel target system. Different targets with various elemental compositions, i.e., Co₂₀Cr₂₀Ni₂₀Mn₂₀Mo₂₀ (target 1), Co₃₀Cr₁₅Ni₂₅Mn₁₅Mo₁₅ (target 2), and Co₁₅Cr₂₅Cu₂₀Mn₂₀Ni₂₀ (target 3), are designed to modify the phase structure. The elemental composition is varied to ensure face-centered cubic (FCC) or body-centered cubic (BCC) phase stabilization. In target 1, the FCC and BCC phases coexist, whereas targets 2 and 3 are characterized by a single FCC phase. Thin films based on targets 1 and 2 exhibit crystalline phases followed by annealing, as indicated by X-ray diffraction (XRD) and transmission electron microscopy (TEM) analyses. In contrast, target 3 yields crystalline thin films without any heat treatment. The thin-film coatings are classified based on the atomic size difference (δ). The δ value for the target with the elemental composition CoCrMoMnNi is 9.7, i.e., ≥ 6.6 , corresponding to an HEA with an amorphous phase. However, the annealed thin film is considered a multiprincipal elemental alloy. In contrast, δ for the CoCrCuMnNi HEA is 5, i.e., ≤ 6.6 , upon the substitution of Mo with Cu, and a solid solution phase is formed without any heat treatment. Thus, the degree of crystallinity can be controlled through heat treatment and the manipulation of δ in the absence of heat treatment. The XRD results clarify the crystallinity and phase structure, indicating the presence of FCC or a combination of FCC and BCC phases. The outcomes are consistent with those obtained through the analysis of the valence electron concentration based on X-ray photoelectron spectroscopy. Furthermore, a selected area electron diffraction analysis confirms the presence of both amorphous and crystalline structures in the HEA thin films. Additionally, phase evolution and segregation are observed at 500 °C.



1. INTRODUCTION

The discovery of high-entropy alloys (HEAs) by Yeh et al. has promoted the development of new concepts and fresh perspectives on alloy design within the emerging era of HEAs.^{1–4} HEAs consist of five or more principal elements with equal or nearly equal atomic ratios and form single-phase solid solutions. The concentration of each element in HEA typically lies in the range of 5–35 atom %;^{5,6} however, some HEAs may also contain minor elements with concentrations below 5 atom %.⁵ In equimolar HEAs, each element has an equal probability of occupying lattice sites in the crystal structure.⁷ In the 21st century, HEAs stand out as a novel material with numerous benefits.⁸ These alloys offer notable advantages, including outstanding resistance to corrosion and oxidation, along with impressive mechanical properties.⁸ Films made from high-entropy alloys (HEAs) showcase these favorable properties while often presenting lower material costs compared to their bulk counterparts. This makes HEA films an economically attractive option for various applications.⁸ The synthesis phenomena for thin-film composition design of HEAs are similar to those of bulk HEAs. Both have base and functional

elements, which can be tailored based on required applications.⁹ Furthermore, nonmetallic elements can be introduced to fill the interstitial site to improve the hardness properties.⁹ The presence of numerous elements in HEAs results in a high configurational entropy, leading to their thermal stability being superior to that of conventional alloys (CAs).¹⁰ Other prominent features distinguishing HEAs from CAs in a wide temperature range include sluggish diffusion and lattice distortion.¹¹ The joint effects of these factors affect the corrosion resistance, tribocorrosion tendencies, strength, hardness, ductility, oxidation/wear, and erosion resistance. The determination of phase selection in HEAs is primarily rationalized based on statistically arranged thermodynamic ranges for most critical parameters. Additionally, researchers

Received: October 5, 2023

Revised: December 11, 2023

Accepted: December 13, 2023

Published: December 26, 2023



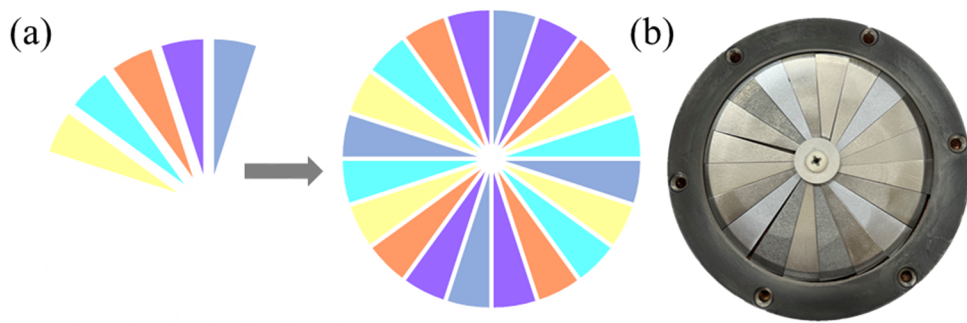


Figure 1. (a) Schematic and (b) digital photograph of the target configurations.

have highlighted that the high mixing entropy is a key factor resulting in the formation of HEA. Specifically, a high mixing entropy promotes the formation of solid solution phases by lowering the Gibbs free energy, as opposed to complex-structured phases such as intermetallic compounds. However, a statistical analysis of thermodynamic parameters for various HEAs has indicated that in addition to high mixing entropy, the atomic size difference (δ) and enthalpy of mixing (ΔH_{mix}) influence the phase selection.¹¹

In CAs, the matrix is typically considered the primary element, and additional elements are then introduced to enhance the strength by modifying the grain boundaries. However, the introduction of secondary elements may result in the formation of several undesired phases, such as intermetallic compounds, which may render the alloys brittle.¹² With the emergence of new technologies in aerospace, electronics, communication, and aviation sectors, there is a growing demand for alloy properties that surpass the capabilities of CAs.^{13–16} Owing to their superior intrinsic properties, ongoing research has focused on the development of HEAs with optimized strength. Several synthesis techniques, such as solid-state processing, mechanical alloying, arc melting, induction melting, casting, and magnetron sputtering, have been used to prepare HEAs. These wide synthesis routes are either considered physical (physical vapor deposition, including vacuum sputtering, vacuum evaporation, and ion plating) or chemical (chemical vapor deposition (CVD) and the liquid phase deposition) synthesis routes.⁹ In this study, the radio frequency (RF) magnetron sputtering strategy is used because it is more efficient than other types of physical vapor deposition (PVD) techniques. In RF magnetron sputtering, atoms are individually etched through a cascade of collisions, resulting in momentum transfer and thus the sputtering of the target material. Furthermore, the distance between the target and substrate is smaller than that in other PVD methods, resulting in better adhesion and control over film thickness.⁴ In particular, RF magnetron sputtering provides an efficient pathway for preparing CoCrMnMoNi and CoCrMnCuNi HEAs with a wide composition range using a single target facility.

Furthermore, the elemental ratios can be tuned and elements can be replaced as needed. This technique has been previously used to efficiently prepare a wide range of highly crystalline refractory HEAs, such as TiZrNbMoTa and TiMoVWCr.^{11,17} Furthermore, the phase structure, including face-centered cubic (FCC) and mixed FCC and body-centered cubic (BCC) phases, can be controlled by adjusting the valence electron concentration (VEC). Mixed FCC + BCC structures can be synthesized by using target elements in a 1:1

ratio (Co₂₀Cr₂₀Mo₂₀Mn₂₀Ni₂₀ (target 1)). Single-phase FCC is obtained in target 2 by increasing the proportions of Co and Ni as FCC phase stabilizers.^{18,19} Similarly, an FCC phase is obtained in target 3 without heat treatment (referred to as WHT in the remaining paper) by reducing δ to ≤ 6.6 , a fundamental criterion to obtain a solid solution. Using the rapid, repeatable, and cost-effective methodology proposed in this paper, future research will be aimed at replacing elements and preparing the HEA coating with controlled elemental ratios for specific applications.

2. EXPERIMENTAL SECTION

2.1. Target Preparation. The target elements were individually purchased from Thifine Korea and then cut into pieces using electrical discharge machining. This process involved the simultaneous arrangement of 20 pieces, as shown in Figure 1a, which were then combined into a single target configuration using a ceramic screw. This innovative approach led to the development of a novel target system, enabling the customization of alloy compositions to meet the specific requirements of various applications requiring HEAs, as demonstrated previously.¹⁷ Furthermore, the precise positioning of each constituent element and the total number of elements played key roles in ensuring a consistent alloy composition. The obtained target elements were polished using emery paper before assembly. In general, to accommodate potential applications, a rapid sputtering procedure and reproducible sputtering targets are essential for replacing or adjusting the target composition.

2.2. Thin-Film Coating. HEA thin films were deposited by RF magnetron sputtering using a configured target. An argon atmosphere was provided as an etchant to sputter the target elements onto a commercially available silicon wafer and Co-Cr substrates to grow the thin films. The samples were ultrasonically cleaned for 10 min each in ethanol and distilled water before the thin-film deposition. The target material segments were polished with emery paper and presputtered for 10 min to remove adherent contaminants. Following target cleaning, the substrates were loaded inside a load lock chamber. To establish a vacuum system and reduce the residual oxygen content, a base pressure of 3×10^{-5} Torr was generated before the thin-film deposition. The thin films were deposited at an RF power of 200 W and a working pressure of 5 mTorr, with high-purity argon gas provided at a flow rate of 30 standard cubic centimeters per minute (SCCM). The RF generator maintained a forward power of 200 W with zero reflected power for 1 h. The substrate temperature was not controlled during the deposition. However, annealing was performed after the deposition for targets 1 and 2.

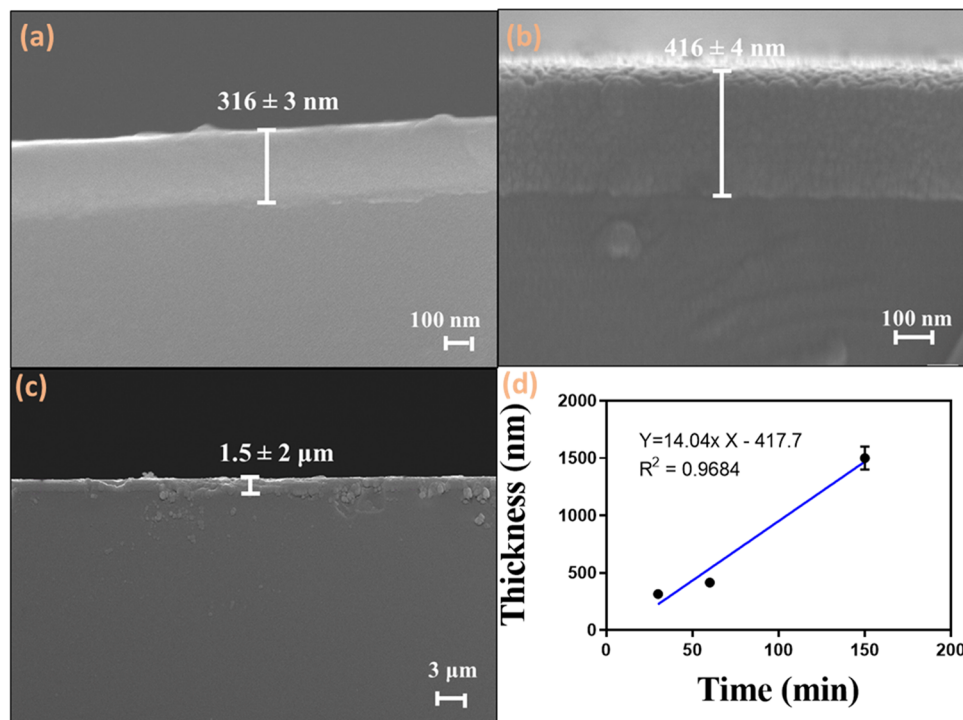


Figure 2. FE-SEM images of HEA thin films deposited for different durations: (a) 30 h, (b) 60 h, and (c) 2.5 h. (d) Graphical representation of the coating thickness as a function of the deposition time.

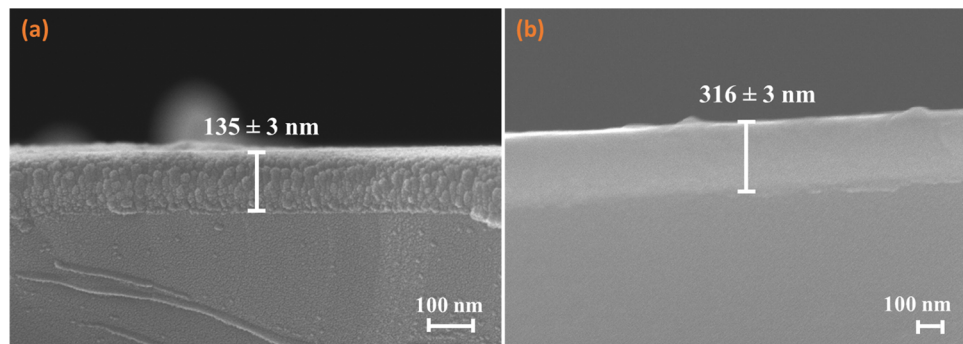


Figure 3. FE-SEM images of HEA thin films deposited at a constant deposition time (30 min) under different working pressures: (a) 2 mTorr and (b) 5 mTorr.

2.3. Thin-Film Characterization. X-ray diffraction (XRD) analysis was performed using Cu K α radiation to assess the crystalline nature and phase structure of the prepared films. The scan rate was maintained at a low value of 1°/min to enhance resolution. The scanning procedure involved a step size of 0.02, an omega value of 1.5°, and a 2 θ range of 10 to 90°. The operational voltage was set at 45 kV. Thickness determination and energy-dispersive spectroscopy (EDS) analysis were based on field-emission scanning electron microscopy (FE-SEM; Gemini 500). The homogeneity of the deposited thin films was evaluated through EDS (Oxford), whereas the surface chemistry and oxidation states before and after argon etching were investigated through X-ray photo-electron spectroscopy (XPS; K-Alpha+ model) with an Al K α X-ray analyzer. Transmission electron microscopy (TEM) was used to analyze the composition and crystallinity.

2.4. Biocompatibility Assay. An A10 cell line was seeded at a confluence of 25% ($5 \times 10^4/\text{mL}$) in 24-well plates. After 3 days, the cell viability was assessed using an MTT (3-(4,

5-dimethylthiazol-2-yl)-2, 5-diphenyltetrazolium bromide) assay, as shown in Figure 14. The cells adhered to the bottom surface over a span of 3 days at a temperature of 37 °C in an environment containing 5% CO₂. Following this incubation period, the culture medium (Dulbecco's Modified Eagle's Medium, DMEM) was removed, and the cells were washed twice using 1× phosphate-buffered saline. Subsequently, a solution containing 0.1 mg/mL MTT was introduced along with a mixture of 540 μL of DMEM growth medium and 60 μL of the MTT assay in each well (constituting a 10% MTT assay). After a two h incubation, the culture medium was replaced with 600 μL of dimethylsulfoxide (DMSO) as the MTT solvent. The cellular viability was assessed by measuring the absorbance at 570 nm by using a Varioskan LUX reader.

3. RESULTS AND DISCUSSION

This paper presents a technique to prepare HEA thin films to eliminate the need for preparing multiple targets. It involves the configuration of the required multitarget elements in a

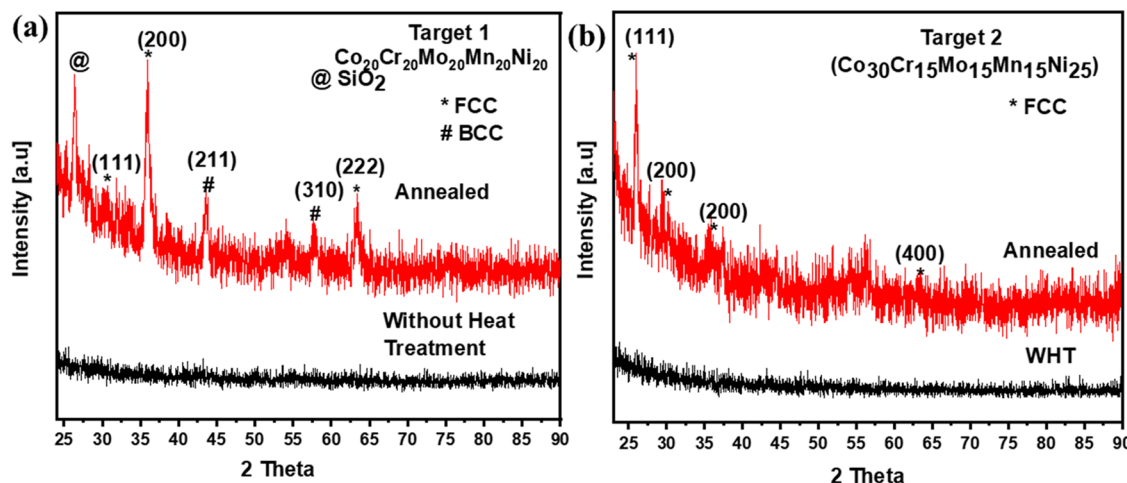


Figure 4. XRD patterns of WHT and heat-treated samples: (a) target 1 and (b) target 2.

Table 1. Parameters for Designing a Solid Solution of HEAs

parameter	reported values	experimental values (CoCrNiMoMn)	experimental values (CoCrNiCuMn)
ΔS_{mix}	$12 \leq \Delta S_{\text{mix}} \geq 17.5 \text{ J/(K mol)}$	13.35 J/(K mol)	12.75 J/(K mol)
ΔH_{mix}	$-15 < \Delta H_{\text{mix}} < 10 \text{ kJ/mol}$	-4.79	-0.952
Ω	$\geq 1.2^{22}$	$5.6 > 1$	$22.61 > 1$
δ	$\leq 6.6\%^{22}$	$8.85 > 6.6$	5.3
VEC	$\text{VEC} \geq 8.0 \text{ (FCC)}^{19}$ $\text{VEC} < 6.87 \text{ (BCC)}^{23}$ $6.87 \leq \text{VEC} < 8.0^{24} \text{ (BCC + FCC)}^{19}$	7.6 (BCC + FCC) 8.2 (FCC)	$9.1 > 8.0 \text{ (FCC)}$

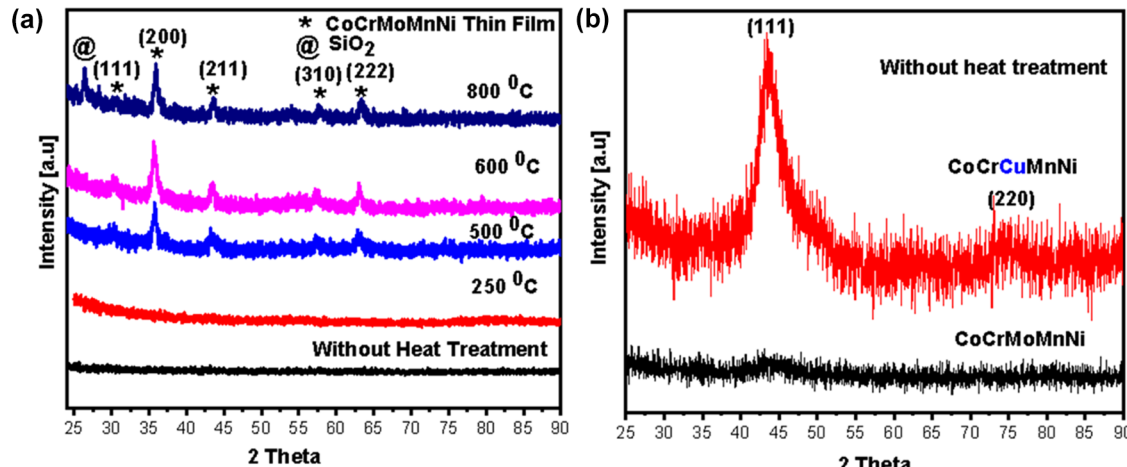


Figure 5. XRD analysis: (A) Effect of annealing at different temperatures, indicating thermal stability. (B) Influence of δ , a criterion for preparing solid solution without heat treatment.

single target system. The use of a configurable target enables the synthesis of diverse HEA thin films for desired applications. Cross-sectional FE-SEM imaging was performed to examine the smoothness of the deposited thin films and measure the change in the film thickness under different deposition durations and working pressures while keeping the other parameters constant. Figures 2 and 3 show the FE-SEM images of HEAs deposited on silicon wafers at different deposition times and working pressures, respectively. Cross-sectional SEM images were recorded to observe the uniformity and homogeneity of the deposited thin films and any irregularities on the top surface. Careful examination of the top surface (Figure 2) confirmed the absence of any crumples on the surfaces. Although the interface was nonuniform (Figure 2c)

because of incorrect cutting of the silicon wafer, the film was smoothly deposited on the top surface of the wafer. As shown in Figure 2a–c, the film thicknesses were 316, 424, and 1.5 μm , respectively. Figure 2d shows that the coating thickness was linearly correlated to the deposition time. The deposition time was increased (Figure 2c) to attain suitable EDS mapping (Figure 12), as proper results could not be achieved for a shorter deposition time. Figure 3 shows that the thin films were smoothly deposited across different working pressures and similar deposition times. The film thickness was 316 nm at a working pressure of 5 mTorr (Figure 3b). However, the cross-sectional thickness reduced to 135 nm when the working pressure was decreased to 2 mTorr, as shown in Figure 3a.

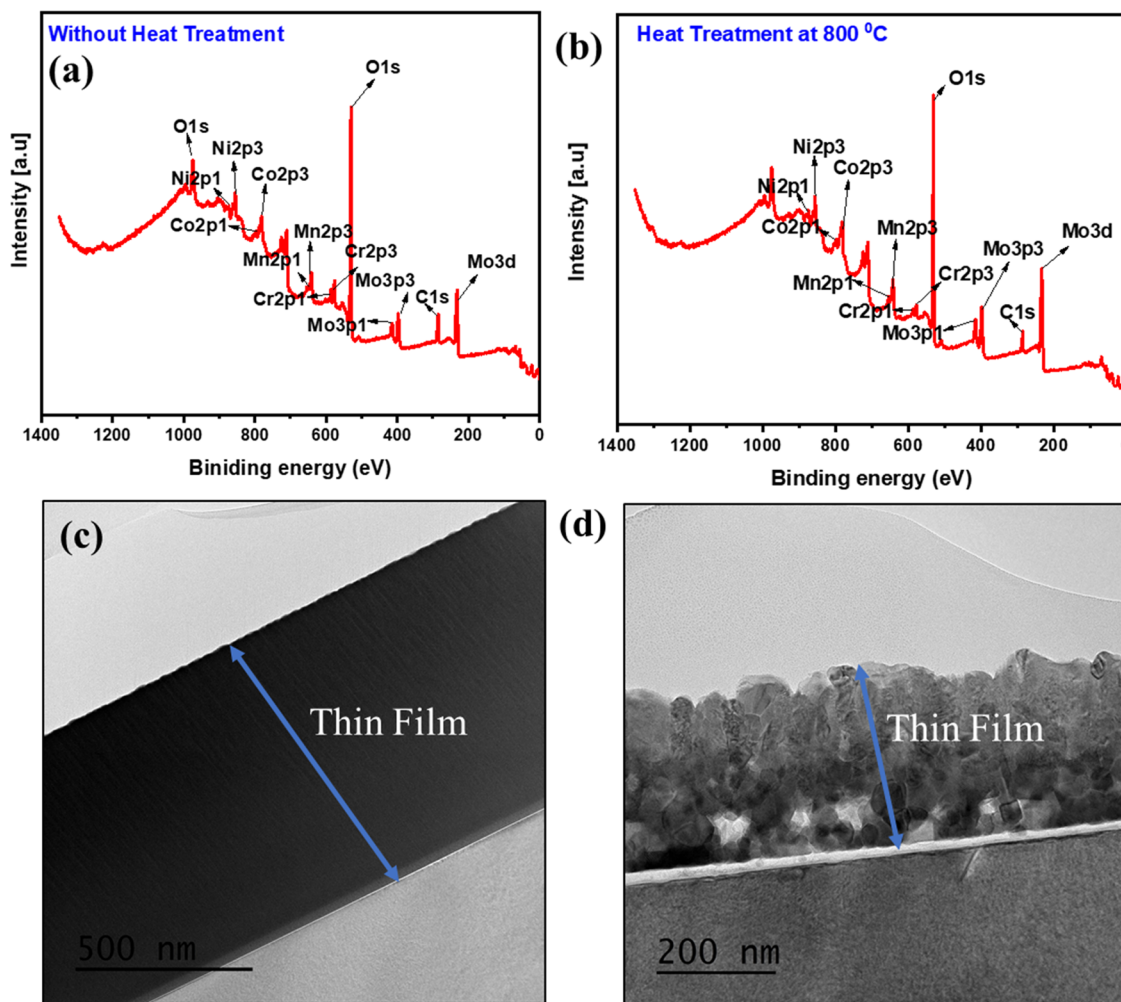


Figure 6. XPS survey spectra of the prepared samples: (a) without heat treatment and (b) with heat treatment at 800 °C. TEM images of the prepared samples: (c) without heat treatment and (d) with heat treatment at 800 °C.

The crystallinity of the prepared samples was examined by using XRD. Figure 4 shows the XRD patterns of the thin films deposited under WHT conditions and those subjected to annealing. The patterns confirmed the amorphous structure of the thin films grown under WHT conditions and a minor crystalline structure of the annealed thin films. These results demonstrated that a more crystalline structure could be synthesized using the proposed target configuration based on a combination of refractory elements, as previously reported.^{11,17} The diffraction data and calculated VECs are summarized in Table 1, indicating that the prepared thin films exhibited dual-phase FCC and BCC as well as single FCC structures. The planes (111), (222), and (200) corresponded to the FCC structure, whereas (200), (211), (310), (222), and (330) were attributable to the BCC structure.

Certain peaks pertaining to SiO₂ were also identified. The effect of one h annealing was investigated. As shown in Figure 5A, thin films synthesized in WHT conditions and at a working temperature of 250 °C were amorphous. In contrast, thin films annealed at various temperatures were crystalline and thermodynamically stable, given the absence of any new phases,⁹ as shown in Figure 5A. Figure 5B shows the XRD peaks of CoCrMnMoNi and CoCrMnCuNi films prepared under WHT conditions. CoCrMnCuNi exhibited a crystalline structure even without annealing. This crystalline structure was

achieved after reducing the δ value to below 6.6, which is a requirement for the synthesis of HEA solid solutions. This adjustment was realized by replacing Mo with Cu. The δ values for CoCrMnMoNi and CoCrMnCuNi were 8.8 > 6.6 and 5.3 < 6.6, respectively (Table 1).

XPS analysis was performed to identify the elemental composition and confirm the successful deposition of the HEAs. Furthermore, we calculated the VEC, a critical parameter for identifying phase structures. Stable FCC phases were formed at VEC ≥ 8.0. The FCC and BCC phases coexisted at 6.87 ≤ VEC < 8.0.^{19,20,21,23} Co, an FCC phase stabilizer, is typically introduced into an alloy system to refine the plasticity without a significant reduction in strength.¹⁸ Co can transform the BCC phase structure into an FCC phase structure, and an increase in the volume fraction of the FCC phase can enhance the plasticity owing to the higher number of slip planes in the FCC phase.¹⁸ Furthermore, Mo, a BCC phase stabilizer, can transform the FCC phase into BCC, thereby increasing the yield strength.²⁴ Similar to Co, Cu also facilitates the formation of the FCC phase structure. However, researchers have widely explored the effect of the Cu element on the structure of HEAs. Due to its high mixing enthalpy, it transforms the phase into dual-phase FCC structure.²⁵ Furthermore, the effect of Al addition into HEAs is BCC type, and if there are both Al and Cu elements in HEAs, then

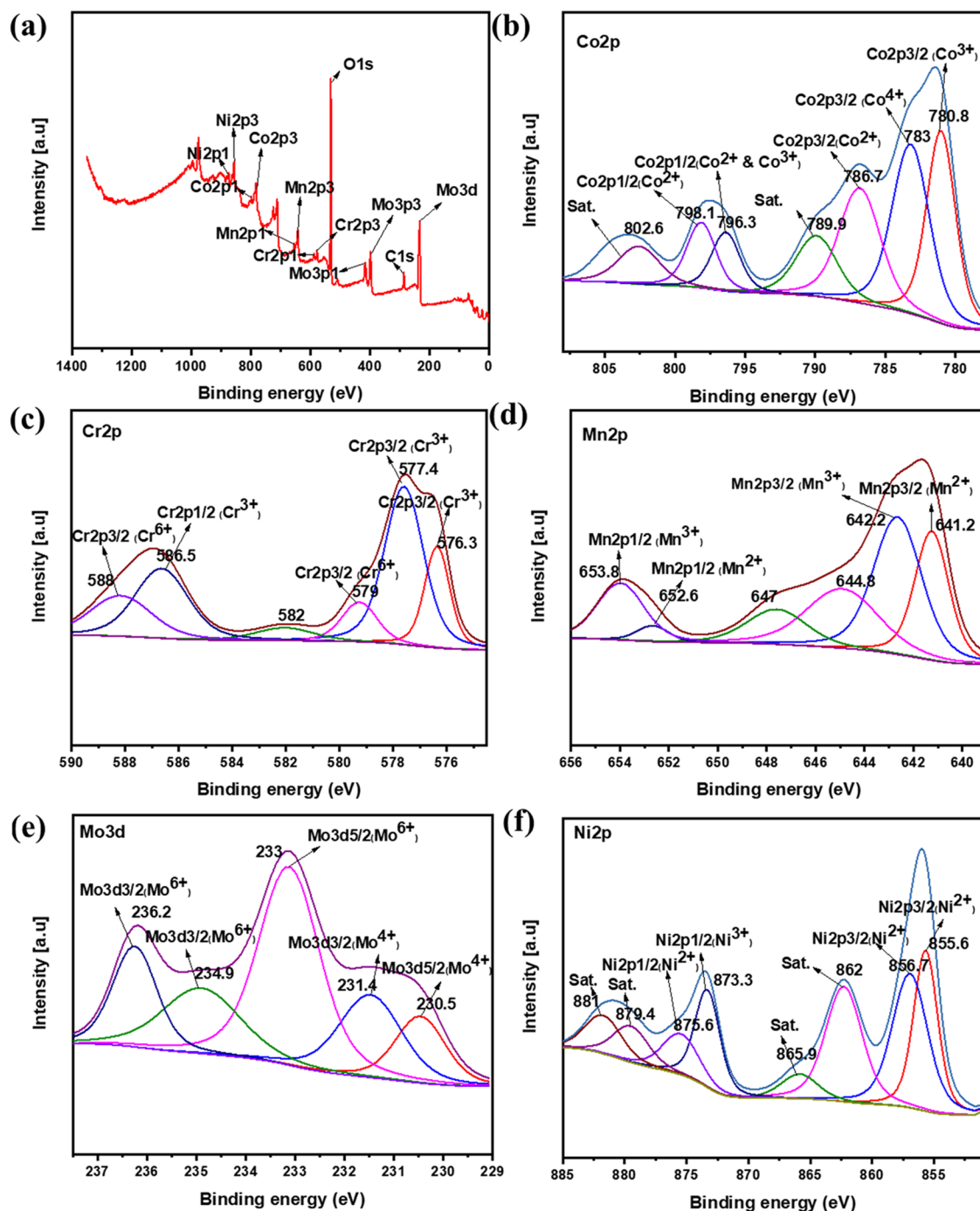


Figure 7. XPS profiles of the prepared HEAs ($\text{Co}_{20}\text{Cr}_{20}\text{Mo}_{20}\text{Mn}_{20}\text{Ni}_{20}$): (a) XPS survey spectra. XPS profiles of (b) Co 2p, (c) Cr 2p, (d) Mn 2p, (e) Mo 3d, and (f) Ni 2p.

the structure transformation depends on the composition of Al element. The research performed by Xu et al.²⁶ explained that with the variation in Al composition, the phase structure changes from BCC to FCC and BCC phase coexistence and into single FCC phase. The structural study on $\text{Al}_x\text{Fe}_2\text{CrNiCu}$ ($x = 0.0, 0.5, 0.75, 1.0, 1.5$) (x in molar ratio) is highlighted, where the BCC phase is obtained at $x = 0.0$ and FCC at $x = 1.5$ and both FCC and BCC dual phases are obtained in intermediate values.²⁶

Figure 6 shows the XPS and TEM results of the samples prepared under WHT conditions and those subjected to annealing. The XPS survey spectra shown in Figure 6a,b

indicate the presence of all of the elements in both samples. Figure 6c,d shows the cross-sectional TEM images, depicting the uniformity and thickness of the thin films.

The XPS survey spectrum shown in Figure 7a confirms the coexistence of all deposited elements in the HEAs, consistent with the outcomes of the TEM and SEM-EDS analyses. XPS peaks corresponding to the substrate were not observed, as the film thickness exceeded >135 nm (the lowest thickness among all the prepared samples), as confirmed by cross-sectional FE-SEM analysis.²⁷ Figure 7b shows two major peaks corresponding to Co at 781.5 and 797 eV, corresponding to $\text{Co} 2p_{3/2}$ and $\text{Co} 2p_{1/2}$, respectively.²⁸ Two satellite peaks were observed at

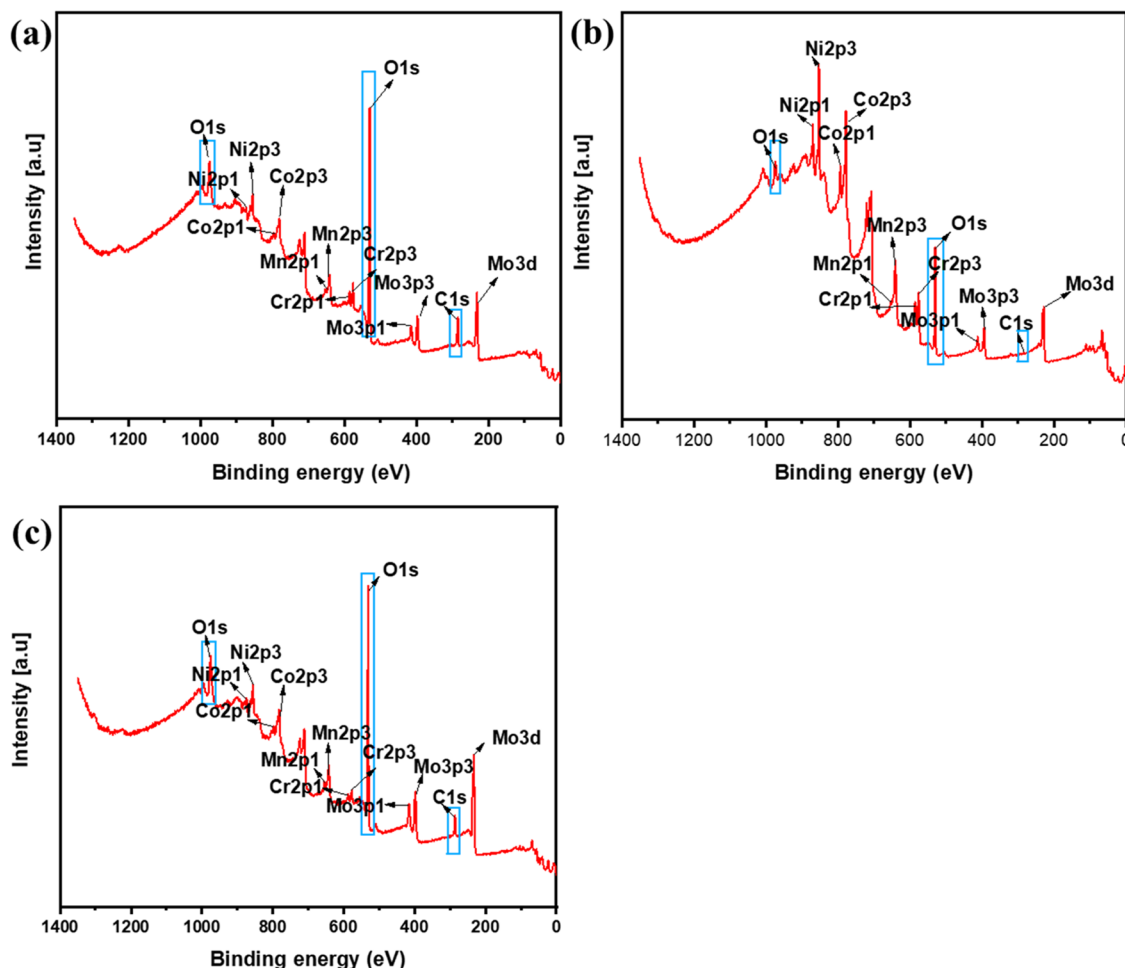


Figure 8. XPS survey spectra of the samples: (a) without argon etching, (b) subjected to argon etching for 17 min, and (c) XPS profile of the heat-treated sample.

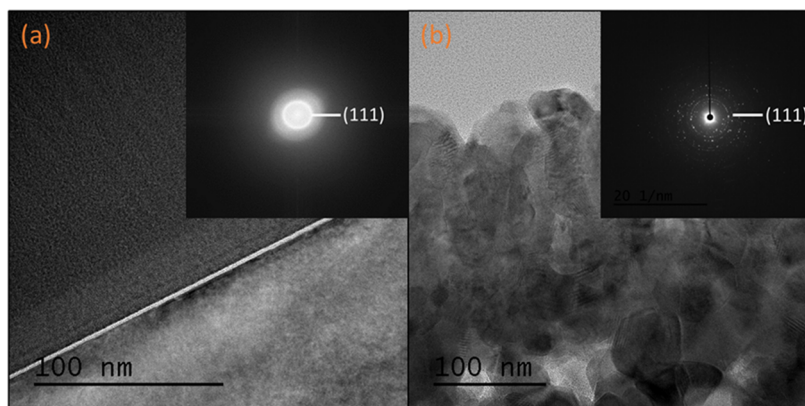


Figure 9. TEM images of the samples: (a) without heat treatment and (b) with heat treatment at 800 °C. The insets provide evidence of the amorphous and polycrystalline structures.

786.7 and 802.6 eV, attributable to the Co^{2+} oxidation state, and another satellite peak at 789.9 eV could be attributed to Co^{3+} .^{28–30} A peak corresponding to Co^{4+} at a binding energy of 783.0 eV was also observed.³¹ The coexistence of Co^{2+} / Co^{3+} mixed valence states could be attributed to the presence of Co_3O_4 .^{32,33} The sharp peaks at 798.1 and 780.8 eV corresponded to Co^{2+} and Co^{3+} .^{34,35} Figure 7c shows XPS peaks at 577 and 586.9 eV, corresponding to $\text{Cr} 2p_{3/2}$ and $\text{Cr} 2p_{1/2}$, respectively. The $\text{Cr} 2p_{3/2}$ peak was deconvoluted into

four peaks centered at 576.3, 577.4, 579.0, and 582.0 eV. Similarly, the $\text{Cr} 2p_{1/2}$ peak was deconvoluted into two peaks at 586.5 and 588 eV. The peaks at 576.3, 577.4, and 586.5 eV were associated with Cr^{3+} .^{36–38} The peaks centered at 579.0 and 588.0 eV were attributable to Cr^{6+} , indicating a higher oxidation state.^{37,39}

Figure 7d shows two peaks centered at 641.9 and 653.8 eV, corresponding to $\text{Mn} 2p_{3/2}$ and $\text{Mn} 2p_{1/2}$, respectively. The $\text{Mn} 2p_{3/2}$ peak was deconvoluted into four peaks centered at

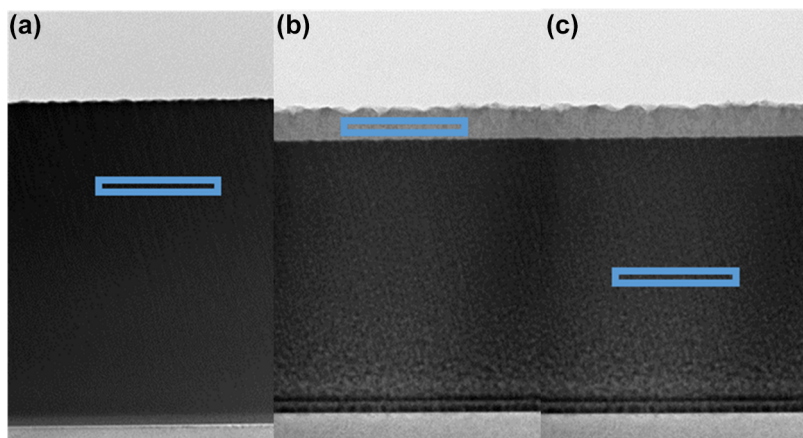


Figure 10. TEM analysis: (A) samples not subjected to heat treatment; (B) surface segregation analysis at 500 °C; and (C) bottom surface analysis at 500 °C, showing no segregation, as indicated in Table 2.

Table 2. Compositional Cross-Verification for Mn Surface Segregation Using TEM and XPS Analyses (All Values in atom %)

elements	no heat treatment atom % (TEM)	heat-treated at 500 °C atom % (TEM surface segregation)	heat-treated at 500 °C (TEM bottom surface)	no heat treatment (XPS)	heat-treated at 500 °C
cobalt	19.9	0.8	22.5	24.5	0
chromium	23.4	0.5	21.8	12.1	0
nickle	22.8	0.4	23.7	16.8	0
manganese	10.0	98.3	5.71	19.3	99.4
molybdenum	23.9	0	26.3	27.4	0.6

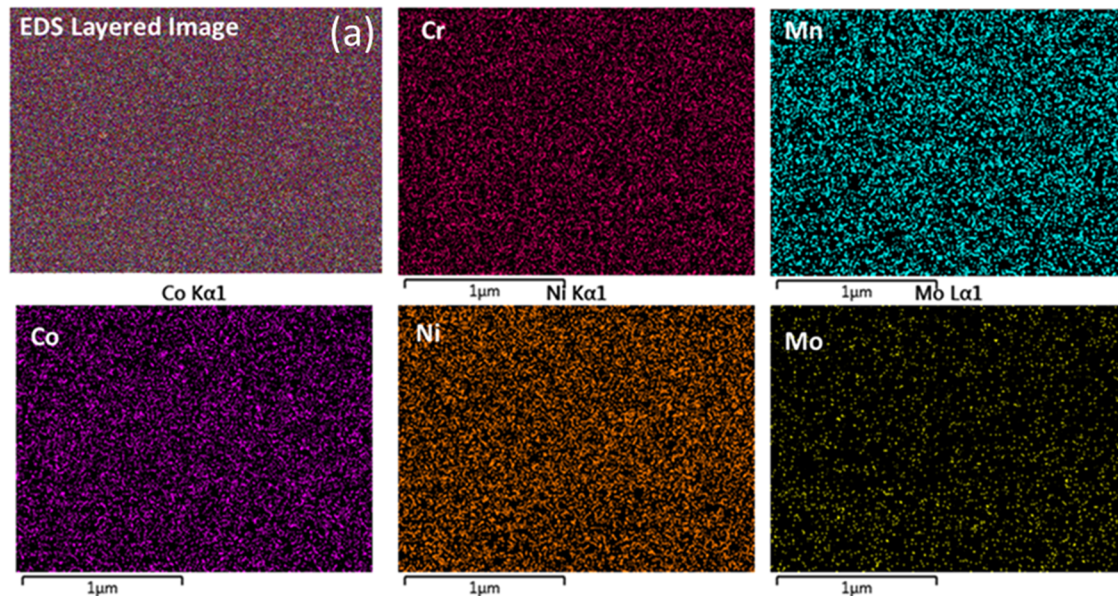


Figure 11. (a) EDS layered mapping of CoCrMoMnNi thin films and the corresponding elements.

641.2, 642.2, 644.8, and 647 eV. The peaks at 641.2, 642.2, and 644.8 eV corresponded to Mn²⁺, Mn³⁺, and Mn⁴⁺, respectively.^{28,40} The Mn 2p_{1/2} peak was deconvoluted into two peaks centered at 652.6 and 653.8 eV, corresponding to Mn²⁺ and Mn³⁺, respectively.²⁸ Similarly, as shown in Figure 7e, the Mo 3d peak was deconvoluted into five peaks centered at 230.5, 231.4, 233, 234.9, and 236.2 eV. The peak at 231.4 eV was attributed to Mo⁴⁺ (3d_{3/2}).⁴¹ The peaks centered at 233.0 (3d_{5/2}), 234.9 (Mo 3d_{5/2}), and 236.2 eV (3d_{3/2}) corresponded to Mo⁶⁺.^{41,42} The 3d_{5/2} peak at 230.4 eV indicated a Mo oxidation state of +4.⁴³ The Ni 2p peak in Figure 6f could be deconvoluted into peaks centered at 855.6, 856.7, 862.0, 865.9,

873.3, 875.6, 879.4, and 881.0 eV with spin-orbit characteristics of either Ni²⁺ or Ni³⁺. The peaks at 855.6 and 856.7 eV corresponded to Ni²⁺, whereas the peak at 873.3 eV was associated with Ni³⁺.^{28,44} Furthermore, two shake-up satellite peaks were observed at binding energies of 862 and 879.4 eV, corresponding to the mixed valence state of Ni.^{16,28} Shake-up satellite peaks were also observed at 865.9 and 881 eV.⁴⁴

The XPS profiles in Figure 8a revealed the presence of the O 1s and C 1s peaks. The peaks of the O 1s and C 1s were considerably reduced through 17 min of argon etching before the XPS analysis (the results are shown in Figure 8b). However, even after argon etching, the peaks of the O 1s and

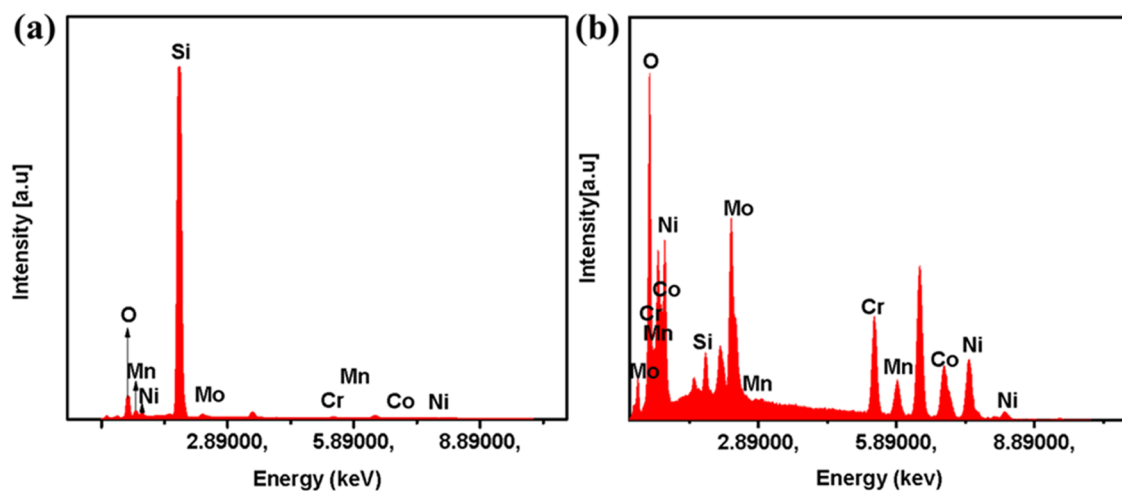


Figure 12. EDS profiles of CoCrMoMnNi HEA thin films deposited at a working pressure of 5 mTorr and deposition times of (a) 1 h and (b) 2.5 h.

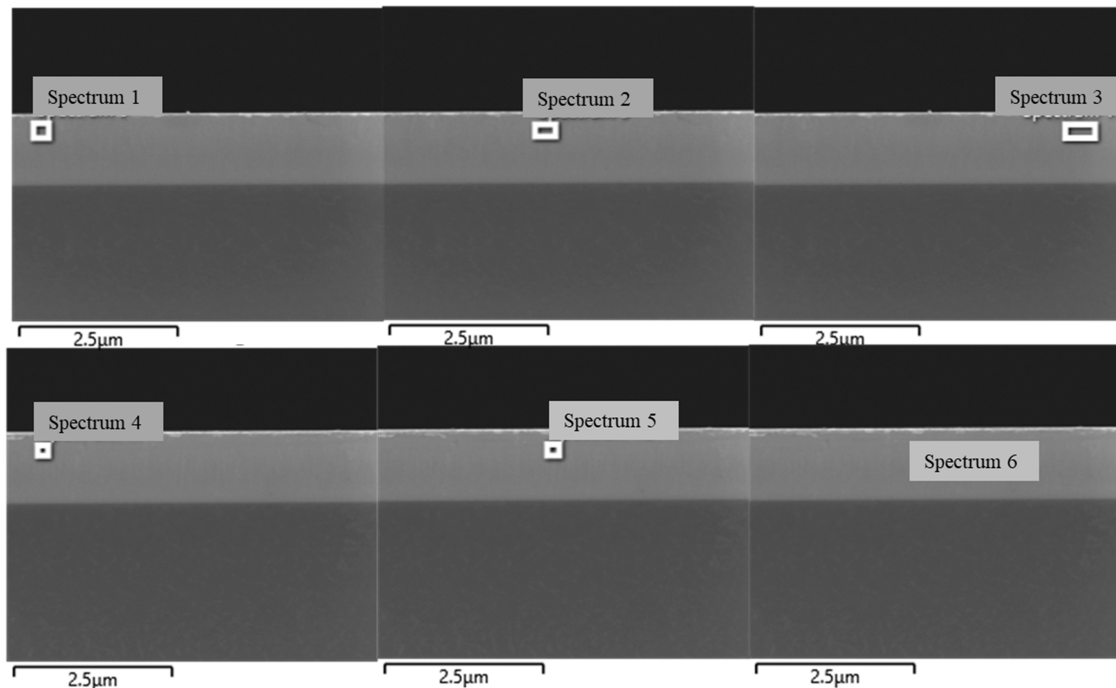


Figure 13. Various spectrum analyzed for homogeneous elemental distribution, as shown in Table 3.

C 1s were observed in the XPS profile of the heat-treated sample, as shown in Figure 8c. Figure 9a,b shows TEM images of the samples prepared under WHT conditions and those subjected to heat treatment, respectively, with the insets indicating amorphous and polycrystalline structures. Both samples exhibited a similar *d*-spacing of 0.20 nm, corresponding to the (111) planes of Co₃O₄ and Ni.^{45,46} The *d*-spacing of 0.24 nm at 800 °C corresponded to that of NiO(111). Tables S1 and S4 present the XPS, TEM, and scanning electron microscopy (SEM)-EDS compositional results of the samples prepared under WHT conditions and those subjected to heat treatment, with elemental concentrations ranging from 5 to 35 atom % (defined concentration range of HEAs), are shown in Tables S1–S4.

Cross-checking of the XPS and TEM-EDS analyses indicated that Mn was preferentially segregated at the top of the surface owing to its limited solid solubility within the

chosen elemental combination, as shown in Figure 10B,C and in Table 2. A similar phase evolution phenomenon has been previously reported.⁴⁷

The elemental mapping and EDS results (Figures 11 and 12) were used to assess the elemental compositions of the deposited solid solutions. As shown in the EDS profiles (Figure 12), the substrate peak was dominant for the sample, with a deposition time of 60 min. This dominance was attributable to the electron beam penetrating deeper into the substrate (1–3 μm)⁴⁸ owing to its low thickness of approximately 424 nm. Therefore, we increased the deposition time to obtain the elemental composition. Figure 12b shows the elemental peaks of the HEA. The substrate peak diminished owing to the larger thickness of the deposited thin films. Furthermore, the EDS analysis was facilitated by horizontally aligning the cut samples with the electron beam, and the results are presented in Table S3. Additionally, in order to examine the uniformity and

Table 3. FE-SEM-EDS Analyses for Various Positions to Confirm a Uniform and Homogeneous Composition

elements	Spec 1	Spec 2	Spec 3	Spec 4	Spec 5	Spec 6	Avg
chromium	22.80	22.62	22.97	22.92	22.63	22.37	22.7
manganese	17.56	17.24	17.40	16.96	17.81	17.53	17.4
cobalt	18.97	19.39	18.66	18.52	19.02	18.98	18.9
nickel	21.30	21.76	21.38	21.81	20.79	21.61	21.4
molybdenum	19.37	18.99	19.58	19.78	19.75	19.52	19.5

homogeneity of the thin-film elements, the prepared coating on the silicon wafer was sectioned and analyzed for composition across multiple spectra as shown in Figure 13. The compositions presented in Table 3 indicate that all elements have been uniformly deposited on the thin film, maintaining homogeneity across the entire film surface.

Various thermodynamic parameters were calculated as follows

$$\delta = \sqrt[100]{\sum_{i=1}^r C_i(1 - r_i/\bar{r})^2} \quad (1)$$

$$\text{where } r = \sum_{i=1}^n C_i r_i$$

$$\Delta H_{\text{mix}} = \sum_{i=1, i \neq j}^n (4\Delta H_{\text{mix}} AB) \quad (2)$$

$$\text{VEC} = \sum_{i=1}^N C_i(\text{VEC})_i \quad (3)$$

$$\Delta S_{\text{mix}} = -R \sum_{i=1}^N C_i \ln c_i \quad (4)$$

$$\Omega = \frac{T_m \Delta S_{\text{mix}}}{\Delta H_{\text{mix}}} \quad (5)$$

$$\text{where } T_m = \sum_{i=1}^N C_i(T_m)_i$$

Furthermore, the values listed for binary elements in Tables 4 and 5 are used in eq 2

Table 4. Mixing Enthalpy $\Delta H_{i,j}$ Calculated Using Miedema's Model for the $i-j$ Atomic Pair for CoCrMoMnNi⁴⁹

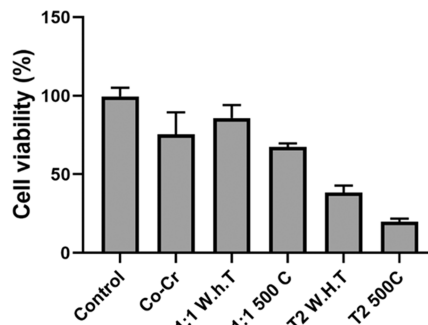
Co	Cr	Mo	Mn	Ni
Co	-4	-5	-5	0
Cr		0	2	-7
Mo			5	-7
Mn				-8
Ni				

Table 5. Mixing Enthalpy $\Delta H_{i,j}$ Calculated Using Miedema's Model for the $i-j$ Atomic Pair for CoCrCuMnNi⁴⁹

Co	Cr	Cu	Mn	Ni
Co	-4	6	-5	0
Cr			2	-7
Cu				4
Mn				-8
Ni				

The biocompatibility of HEAs with different compositions, both annealed and under WHT conditions, was evaluated with

that of untreated L605 Co–Cr. An A10 cell line was seeded at a confluence of 25% ($5 \times 10^4/\text{m}$). Three days later, the cell viability was assessed using the MTT assay, as shown in Figure 14. The biocompatibility of target 1 was superior to that of

**Figure 14.** MTT assay analysis for the A10 cells.

other modified surfaces as well as Co–Cr. Notably, Co–Cr is of interest as a stent material.^{50,51} Thus, Co–Cr samples were further modified with the CoCrMoMnNi HEA for potential biological applications. It is considered by researchers that Ni element is harmful and causes allergy to the human body.⁵² In our study, we used a Ni-containing HEA to further investigate the Ni toxicity. The reason behind using Ni-based alloy is that though Ni is toxic, however Ni based HEAs like TiAlFeCoNi exhibit much better cellular metabolic activity in contrast to Ti.⁵³ Similarly, another type of Ni-based NiCrMo alloy is more commonly used in orthopedic and dental implants. The NiCrMo alloy, when employed as an implant, underwent examination.⁵⁴ The study revealed the formation of new bone tissues in the vicinity of the implants, and importantly, no signs of inflammation or adverse reactions were observed in both the existing and newly formed tissues.⁵⁴ Furthermore, high cell viability obtained in this research is attributed to the high oxide layer on the surface of the coatings as analyzed by XPS. The oxide layer promotes the formation of highly stable oxide layers due to its passivation and improves cell viability.¹¹ Thus, highly oxide-generated surfaces, modified with a thin film using elements of 1:1 in target 1, showed better cell viability. Additionally, the biocompatibility could be attributed to the stable oxide layer as it prevents the release of toxic ions.¹¹ The intricate mechanisms underlying the toxicity of cobalt (Co), nickel (Ni), and manganese (Mn) are complicated and not fully understood.⁵⁵ The prevalent oxidation state for nickel (Ni) is Ni^{2+} , although nickel has the flexibility to exhibit oxidation states ranging from -1 to +4. Ni appears to be an essential metal for humans due to its biological prevalence. Deficiencies in nickel (Ni) in animals have been associated with various issues, such as reduced growth, hindered iron absorption, and diminished activity in multiple metabolic pathways.⁵⁵ These findings suggest that nickel may indeed play a role in the biochemical processes of complex organisms.

Hence, there is a possibility that nickel (Ni) is indirectly essential for humans, potentially supporting the growth and development of mutualistic microbes.⁵⁵ Due to some reports regarding side effects and allergy to the human body, still further research is required to fully understand the behavior of Ni-based HEAs as a biocompatibility.

4. CONCLUSIONS

HEAs consisting of CoCrNiMnMo and CoCrNiMnCu were synthesized by using an RF magnetron sputtering system with various elemental compositions. The results demonstrated the applicability of RF sputtering that could be used for a combination of multiple elements in a single target system. The proposed method can enable elemental substitution and preparation of a wide range of HEAs. Cross-sectional FE-SEM images revealed that thin films were smoothly deposited with laminar cross-sectional growth. The XRD analysis distinguished amorphous films deposited under WHT conditions and crystalline films prepared by heat treatment and adjustment of δ . The surface elemental composition was analyzed by XPS, further confirming the phase structure, which included mixed FCC-BCC and only FCC phases. The VEC results were consistent with the XRD results, demonstrating the coexistence of peaks corresponding to both the FCC and BCC phases as well as the occurrence of single-phase structures while tuning the elemental ratios. Compositional analysis was performed using XPS, TEM, and SEM-EDS in the elemental concentration range of 5–35 atom %. Notably, the substrate modified with target 1 exhibited significantly improved cell viability compared with other thin-film coatings under various conditions. The proposed target preparation method can be extended to prepare a wide range of medium-entropy alloys and HEAs for various applications requiring different elemental compositions and phase structures. Future work will be aimed at clarifying the relationships between different elements and configuring our target system with different elemental compositions to satisfy the requirements of various applications.

■ ASSOCIATED CONTENT

SI Supporting Information

The Supporting Information is available free of charge at <https://pubs.acs.org/doi/10.1021/acsomega.3c07721>.

Additional compositional analysis for all the targets are provided in Supporting Information. The XPS, TEM, and EDS analyses without heat treatment and with heat treatment performed at 800 °C. Compositions analyzed are compared and found that SEM cross-sectional analysis is the more appropriate option in comparison to XPS analysis ([PDF](#))

■ AUTHOR INFORMATION

Corresponding Authors

Tae-Hoon Kim – School of Materials Science & Engineering, Chonnam National University, Gwangju 61186, Republic of Korea; Email: thk@jnu.ac.kr

Hoonsung Cho – School of Materials Science & Engineering, Chonnam National University, Gwangju 61186, Republic of Korea; Email: cho.hoonsung@jnu.ac.kr

Authors

Khurshed Alam – School of Materials Science & Engineering, Chonnam National University, Gwangju 61186, Republic of Korea; Department of Metal Powder, Korea Institute of Materials Science, 51508 Changwon, South Korea;
DOI: orcid.org/0000-0001-8115-4711

Woohyung Jang – Department of Prosthodontics, School of Dentistry, Chonnam National University, Gwangju 61186, Korea

Geonwoo Jeong – School of Materials Science & Engineering, Chonnam National University, Gwangju 61186, Republic of Korea

Jinhui Ser – School of Materials Science & Engineering, Chonnam National University, Gwangju 61186, Republic of Korea; Gordon Center for Medical Imaging, Department of Radiology, Massachusetts General Hospital and Harvard Medical School, Boston, Massachusetts 02114, United States

Doori Kang – School of Materials Science & Engineering, Chonnam National University, Gwangju 61186, Republic of Korea

Complete contact information is available at:
<https://pubs.acs.org/10.1021/acsomega.3c07721>

Author Contributions

[†]K.A. and W.J. contributed equally to this work.

Notes

The authors declare no competing financial interest.

■ ACKNOWLEDGMENTS

This research was supported by the Basic Science Research Program through the National Research Foundation of Korea (NRF) funded by the Ministry of Education (No. 2021R1I1A1A01058691) and by the National Research Foundation of Korea (NRF) grant funded by the Korea Government (MSIT) (No. 2021R1F1A1064062).

■ REFERENCES

- (1) Yeh, J. W.; Chen, S.; Lin, S.; et al. Nanostructured high-entropy alloys with multiple principal elements: novel alloy design concepts and outcomes. *Adv. Eng. Mater.* **2004**, *6* (5), 299–303.
- (2) Biswas, K.; Yeh, J. W.; Bhattacharjee, P. P.; et al. High entropy alloys: Key issues under passionate debate. *Scr. Mater.* **2020**, *188*, 54–58.
- (3) Cantor, B.; Chang, I.; Knight, P.; et al. Microstructural development in equiatomic multicomponent alloys. *Mater. Sci. Eng., A* **2004**, *375-377*, 213–218.
- (4) Oluwatosin Abegunde, O.; Titilayo Akinlabi, E.; Philip Oladijo, O.; et al. Overview of thin film deposition techniques. *AIMS Mater. Sci.* **2019**, *6* (2), 174–199.
- (5) Tsai, M.-H.; Yeh, J.-W. High-entropy alloys: a critical review. *Mater. Res. Lett.* **2014**, *2* (3), 107–123.
- (6) Usman, K.; Kang, D.; Jeong, G.; et al. The Surface Properties of Implant Materials by Deposition of High-Entropy Alloys (HEAs). *Nanomaterials* **2023**, *13*, 1123.
- (7) Alvi, S.; Jarzabek, D. M.; Kohan, M. G.; et al. Synthesis and Mechanical Characterization of a CuMoTaWV High-Entropy Film by Magnetron Sputtering. *ACS Appl. Mater. Interfaces* **2020**, *12* (18), 21070–21079.
- (8) Zhao, H.; Zheng, Z.; Jiang, T.; et al. High entropy alloy thin films on SS304 substrates: Evolution of microstructure and interface modulated by energetic condensation in nanoscale. *Mater. Des.* **2023**, *230*, No. 111981.
- (9) Yan, X. H.; Li, J. S.; Zhang, W. R.; et al. A brief review of high-entropy films. *Mater. Chem. Phys.* **2018**, *210*, 12–19.

- (10) An, Z.; Jia, H.; Wu, Y.; et al. Solid-solution CrCoCuFeNi high-entropy alloy thin films synthesized by sputter deposition. *Mater. Res. Lett.* **2015**, *3* (4), 203–209.
- (11) Alam, K.; Jeong, G.; Jang, W.; et al. Enhanced mechanical properties and in vitro biocompatibility of TiMOVWCr high-entropy alloy synthesized by magnetron sputtering. *Appl. Surf. Sci.* **2023**, *639*, No. 158222.
- (12) Alshataif, Y. A.; et al. Manufacturing Methods, Microstructural and Mechanical Properties Evolutions of High-Entropy Alloys: A Review. *Met. Mater. Int.* **2019**, *1099*–1133.
- (13) Zhou, H.; He, J. Synthesis of the New High Entropy Alloy and Its Application in Energy Conversion and Storage. *Front. Energy Res.* **2020**, *8*, No. 73, DOI: [10.3389/fenrg.2020.00073](https://doi.org/10.3389/fenrg.2020.00073).
- (14) Khan, M. M.; Rahman, Z. U.; Deen, K. M.; et al. Sputtered Mg_{100-x}Znx (0 ≤ x ≤ 100) systems as anode materials for a biodegradable battery aimed for transient bioelectronics. *Electrochim. Acta* **2020**, *329*, No. 135129.
- (15) Khan, M. M.; Shabib, I.; Haider, W. A combinatorially developed Zr-Ti-Fe-Al metallic glass with outstanding corrosion resistance for implantable medical devices. *Scr. Mater.* **2019**, *162*, 223–229.
- (16) Khan, M. M.; Deen, K. M.; Haider, W. Combinatorial development and assessment of a Zr-based metallic glass for prospective biomedical applications. *J. Non-Cryst. Solids* **2019**, *523*, No. 119544.
- (17) Alam, K.; Jang, W.; Jeong, G.; et al. Design and Development of High-Entropy Alloys with a Tailored Composition and Phase Structure Based on Thermodynamic Parameters and Film Thickness Using a Novel Combinatorial Target. *ACS Omega* **2023**, *8* (31), 28333–28343.
- (18) Qin, G.; et al. Effect of Co content on phase formation and mechanical properties of (AlCoCrFeNi)_{100-x}Cox high-entropy alloys. *Mater. Sci. Eng., A* **2018**, *710*, 200–205.
- (19) Guo, S.; Ng, C.; Lu, J.; et al. Effect of valence electron concentration on stability of fcc or bcc phase in high entropy alloys. *J. Appl. Phys.* **2011**, *109* (10), No. 103505.
- (20) Gao, M. C. et al. *High-Entropy Alloys: Fundamentals and Applications*; Springer, 2016.
- (21) Ye, Y. F.; Wang, Q.; Lu, J.; et al. High-entropy alloy: challenges and prospects. *Mater. Today* **2016**, *19* (6), 349–362.
- (22) Yang, X.; Zhang, Y. Prediction of high-entropy stabilized solid-solution in multi-component alloys. *Mater. Chem. Phys.* **2012**, *132* (2–3), 233–238.
- (23) Chang, X.; Zeng, M.; Liu, K.; et al. Phase Engineering of High-Entropy Alloys. *Adv. Mater.* **2020**, *32* (14), No. 1907226.
- (24) Chen, R.; Qin, G.; Zheng, H.; et al. Composition design of high entropy alloys using the valence electron concentration to balance strength and ductility. *Acta Mater.* **2018**, *144*, 129–137.
- (25) Hu, Q.; et al. Effects of Cu additions on microstructure and mechanical properties of as-cast CrFeCoNiCux high-entropy alloy. *Trans. Nonferrous Met. Soc. China* **2023**, *33* (6), 1803–1813.
- (26) Xu, C.; Geng, N.; Xiang, Q.; et al. A novel dual phase high entropy casting alloy with high damping capacity. *Mater. Res. Express* **2021**, *8* (4), No. 046517.
- (27) Cabrera-German, D.; Gomez-Sosa, G.; Herrera-Gomez, A. Accurate peak fitting and subsequent quantitative composition analysis of the spectrum of Co 2p obtained with Al K α radiation: I: cobalt spinel. *Surf. Interface Anal.* **2016**, *48* (5), 252–256.
- (28) Wang, D.; Liu, Z.; Du, S.; et al. Low-temperature synthesis of small-sized high-entropy oxides for water oxidation. *J. Mater. Chem. A* **2019**, *7* (42), 24211–24216.
- (29) Yu, Z.; Hao, J.; Li, W.; et al. Enhanced Electrochemical Performances of Cobalt-Doped Li₂MoO₃ Cathode Materials. *Materials* **2019**, *12* (6), No. 843, DOI: [10.3390/ma12060843](https://doi.org/10.3390/ma12060843).
- (30) Han, X.; et al. Design of porous cobalt sulfide nanosheets array on Ni foam from zeolitic imidazolate frameworks as an advanced electrode for supercapacitors. *Nanoscale* **2017**, *10*, 2735–2741, DOI: [10.1039/C7NR07931A](https://doi.org/10.1039/C7NR07931A).
- (31) Zhang, J.; Meng, D.; Huang, H.; et al. Phase competition in the growth of SrCoO_x/LaAlO₃ thin films. *AIP Adv.* **2018**, *8* (2), No. 025322.
- (32) Wu, W.; Zhang, Q.; Wang, X.; et al. Enhancing Selective Photooxidation through Co-Nx-doped Carbon Materials as Singlet Oxygen Photosensitizers. *ACS Catal.* **2017**, *7*, 7267–7273, DOI: [10.1021/acscatal.7b01671](https://doi.org/10.1021/acscatal.7b01671).
- (33) Serment, B.; Brochon, C.; Hadzioannou, G.; et al. The versatile Co²⁺/Co³⁺ oxidation states in cobalt alumina spinel: how to design strong blue nanometric pigments for color electrophoretic display. *RSC Adv.* **2019**, *9* (59), 34125–34135.
- (34) Smyrnioti, M.; Ioannides, T. Synthesis of Cobalt-Based Nanomaterials from Organic Precursors. In *Cobalt*; IntechOpen, 2017.
- (35) Sun, Z.; Yuan, M.; Lin, L.; et al. Needle grass-like cobalt hydrogen phosphate on Ni foam as an effective and stable electrocatalyst for the oxygen evolution reaction. *Chem. Commun.* **2019**, *55* (65), 9729–9732.
- (36) Bao, B.; Liu, J.; Xu, H.; et al. Insight into a high temperature selective oxidation of HP40 alloy under a H₂–H₂O environment. *RSC Adv.* **2017**, *7* (14), 8589–8597.
- (37) Bumajdad, A.; Al-Ghareeb, S.; Madkour, M.; et al. Non-noble, efficient catalyst of unsupported α -Cr₂O₃ nanoparticles for low temperature CO Oxidation. *Sci. Rep.* **2017**, *7* (1), No. 14788.
- (38) Bandara, P. C.; Peña-Bahamonde, J.; Rodrigues, D. F. Redox mechanisms of conversion of Cr(VI) to Cr(III) by graphene oxide-polymer composite. *Sci. Rep.* **2020**, *10* (1), No. 9237.
- (39) Wang, H.; Zhang, M.; Lv, Q. Removal efficiency and mechanism of Cr (VI) from aqueous solution by maize straw biochars derived at different pyrolysis temperatures. *Water* **2019**, *11* (4), 781.
- (40) Li, X.; Xin, M.; Guo, S.; et al. Insight of synergistic effect of different active metal ions in layered double hydroxides on their electrochemical behaviors. *Electrochim. Acta* **2017**, *253*, 302–310, DOI: [10.1016/j.electacta.2017.09.075](https://doi.org/10.1016/j.electacta.2017.09.075).
- (41) Zhao, L.; Jia, J.; Yang, Z.; et al. One-step synthesis of CdS nanoparticles/MoS₂ nanosheets heterostructure on porous molybdenum sheet for enhanced photocatalytic H₂ evolution. *Appl. Catal., B* **2017**, *210*, 290–296.
- (42) De Melo, O.; García-Pelayo, L.; González, Y.; et al. Chemically driven isothermal closed space vapor transport of MoO₂: thin films, flakes and in situ tellurization. *J. Mater. Chem. C* **2018**, *6* (25), 6799–6807.
- (43) Dinda, D.; Ahmed, M. E.; Mandal, S.; et al. Amorphous molybdenum sulfide quantum dots: An efficient hydrogen evolution electrocatalyst in neutral medium. *J. Mater. Chem. A* **2016**, *4*, 15486–15493, DOI: [10.1039/C6TA06101J](https://doi.org/10.1039/C6TA06101J).
- (44) Pandey, D. K.; Ankade, S. B.; Ali, A.; et al. Nickel-catalyzed C–H alkylation of indoles with unactivated alkyl chlorides: evidence of a Ni(i)/Ni(iii) pathway. *Chem. Sci.* **2019**, *10* (41), 9493–9500.
- (45) Hung, S.-F.; Tung, C. W.; Chan, T. S.; et al. In situ morphological transformation and investigation of electrocatalytic properties of cobalt oxide nanostructures toward oxygen evolution. *CrystEngComm* **2016**, *18* (32), 6008–6012.
- (46) Barai, H. R.; Banerjee, A. N.; Joo, S. W. Improved electrochemical properties of highly porous amorphous manganese oxide nanoparticles with crystalline edges for superior supercapacitors. *J. Ind. Eng. Chem.* **2017**, *56*, 212–224.
- (47) Li, Y. J.; Savan, A.; Kostka, A.; et al. Accelerated atomic-scale exploration of phase evolution in compositionally complex materials. *Mater. Horiz.* **2018**, *5* (1), 86–92.
- (48) Vernon-Parry, K. D. Scanning electron microscopy: an introduction. *III-Vs Rev.* **2000**, *13* (4), 40–44.
- (49) Takeuchi, A.; Inoue, A. Classification of bulk metallic glasses by atomic size difference, heat of mixing and period of constituent elements and its application to characterization of the main alloying element. *Mater. Trans.* **2005**, *46* (12), 2817–2829.

- (50) Hagemeister, J.; Baer, F. M.; Schwinger, R. H.; et al. Compliance of a cobalt chromium coronary stent alloy—the COVIS trial. *Curr. Controlled Trials Cardiovasc. Med.* **2005**, *6* (1), No. 17.
- (51) Alam, K.; et al. Synthesis of Graphene Oxide Using Atmospheric Plasma for Prospective Biological Applications. *Int. J. Nanomed.* **2020**, *15*, 5813–5824.
- (52) Zdrojewicz, Z.; Popowicz, E.; Winiarski, J. [Nickel - role in human organism and toxic effects]. *Pol. Merkur Lekarski* **2016**, *41* (242), 115–118.
- (53) Edalati, P.; et al. Ultrahigh hardness and biocompatibility of high-entropy alloy TiAlFeCoNi processed by high-pressure torsion. *Mater. Sci. Eng., C* **2020**, *112*, No. 110908.
- (54) Er, Y.; Unsaldi, E. The production of nickel-chromium-molybdenum alloy with open pore structure as an implant and the investigation of its biocompatibility in vivo. *Adv. Mater. Sci. Eng.* **2013**, *2013*, No. 568479, DOI: [10.1155/2013/568479](https://doi.org/10.1155/2013/568479).
- (55) Sule, K.; Umbasaar, J.; Prenner, E. J. Mechanisms of Co, Ni, and Mn toxicity: From exposure and homeostasis to their interactions with and impact on lipids and biomembranes. *Biochim. Biophys. Acta, Biomembr.* **2020**, *1862* (8), No. 183250.